Standard photoacoustic spectrometer: Model and validation using O_2 *A*-band spectra

K. A. Gillis,[1,a)] D. K. Havey,[1,2] and J. T. Hodges[1]

[1]*Process Measurements Division, National Institute of Standards and Technology, Gaithersburg, Maryland 20899, USA*

[2]*Department of Chemistry and Biochemistry, James Madison University, MSC 4501, Harrisonburg, Virginia 22807, USA*

We model and measure the absolute response of an intensity-modulated photoacoustic spectrometer comprising a 10 cm long resonator and having a Q-factor of approximately 30. We present a detailed theoretical analysis of the system and predict its response as a function of gas properties, resonance frequency, and sample energy transfer relaxation rates. We use a low-power continuous wave laser to probe O_2 *A*-band absorption transitions using atmospheric, humidified air as the sample gas to calibrate the system. This approach provides a convenient and well-characterized method for calibrating the absolute response of the system provided that water-vapor-mediated relaxation effects are properly taken into account. We show that for photoacoustic spectroscopy (PAS) of the O_2 *A*-band, the maximum conversion efficiency of absorbed photon energy to acoustic energy is approximately 40% and is limited by finite collision-induced relaxation rates between the two lowest-lying excited electronic states of O_2. PAS also shows great potential for high-resolution line shape measurements: calculated and experimental values for the PAS system response differ by about 1%. [doi:10.1063/1.3436660]

I. INTRODUCTION

Photoacoustic spectroscopy (PAS) is recognized as a versatile and sensitive optical technique for measuring the absorption coefficient of gases and aerosols.[1–5] Compared to laser measurements based on the Beer–Lambert law of light absorption and transmission, PAS involves an additional energy transfer mechanism, which corresponds to the conversion of absorbed optical power to an acoustic wave whose amplitude is measured with a microphone. Because the acoustic properties of the system (e.g., resonator and microphone responses) do not depend on the spectral distribution of the absorbed radiation, PAS spectrometers are optically broadband devices. PAS also has the benefit of being a zero-background measurement, in contrast to direct absorption spectroscopy. However, the conversion of optical-to-acoustic energy can make the acoustic signal vary nonlinearly with absorber and buffer-gas concentration.[6–8] This and additional complications of the acoustic field often prevent robust prediction of absolute PAS system response over a wide range of gas composition, pressure, and temperature. Typically, the PAS system response is calibrated in terms of a reference sample of known absorption coefficient. PAS systems are often calibrated with the same probe laser and at the same wavelength as those employed for the measurements of interest without a need to disassemble the cell.

The goal of this work is to demonstrate an accurate method for calculating and measuring the absolute response of a laser-driven and acoustically resonant photoacoustic (PA) spectrometer. To this end, we combine first-principles models of acoustic wave propagation with high-resolution spectroscopic measurements. Our measurements exploit the well-known spectroscopic parameters of near-infrared magnetic dipole transitions of the O_2 *A*-band.[9–11] Our method conveniently takes advantage of the known composition of air, and thereby eliminates the uncertainties and difficulties associated with reference sample preparation. Recently, Tian *et al.*[12] discussed a similar approach in which the known optical absorption properties of the O_2 *A*-band were used to calibrate the response of a PAS system. However, they did not consider the effects of molecular relaxation. In contrast to their work, our measurements at audio frequencies show that the efficiency of energy conversion from excited electronic states of O_2 (caused by absorption of light in the O_2 *A*-band) to translational states (acoustic energy) is less than unity and depends on the amount of water present. Moreover, this conversion efficiency is low for dry air, increases as the water content increases, and reaches a maximum value of approximately 0.4 for mole fractions of water above 0.01. Therefore, failure to account for the reduced conversion efficiency results in a large systematic error.

In the following, we summarize the underlying theory of acoustic wave generation and propagation with a focus on resonators driven by the absorption of laser radiation. We describe a new PA resonator,[13] which we propose could be adopted as a standard system suitable for laboratory and field measurements of absorption coefficient, and we model its response as a function of gas properties, resonance frequency, and sample energy transfer relaxation rates. We present spectrally resolved PAS absorption measurements of

---

a)Author to whom correspondence should be addressed. Electronic mail: keith.gillis@nist.gov.

O_2 A-band transitions in room temperature air over a wide range of humidity levels probed with a single-mode, tunable, intensity-modulated, continuous-wave laser. Finally, we report the cell constant and its combined uncertainty, and we discuss the potential of our approach to standardize PAS measurements.

II. THEORY OF PHOTOACOUSTIC RESONATORS

This section defines our notation and describes the physical principles involved in PA sound generation and detection within a gas-filled cavity. We applied these general principles in order to design a PA resonator and to model its frequency response as described in the next section. We restrict our considerations to the interaction between intensity-modulated, continuous-wave laser light and a gas containing an absorbing species. Detailed discussions of PA theory that are outside the scope of this paper may be found in the literature.[14,15] First, we discuss the absorption of optical energy as a sound source and include the effects of slow relaxation from the excited state. Second, we discuss the acoustic response of the gas in the cavity due to the PA source. The effect of bulk viscosity, i.e., dispersion and attenuation of sound propagation due to molecular relaxation, on the frequency response is discussed briefly.

A. Sound generation from light absorption

The theoretical development is based on several assumptions about the optical light. (1) We assume spectrally pure laser light at frequency ν. In practice, this assumption requires that the spectral bandwidth is small compared to any absorption features to be studied. (2) The laser's output optical power W is amplitude modulated between zero and W_{pk} with sinusoidal time dependence at frequency $f = \omega/2\pi$, i.e., $W(t) = \frac{1}{2}W_{pk}[1 + \cos(\omega t)]$. The oscillating portion of the power has amplitude $W_0 = \frac{1}{2}W_{pk}$, and it alone contributes to the PA signal. For the theoretical development, we assume that the explicit time dependence is $e^{i\omega t}$, and we keep in mind that the physical time-dependent quantities are given by the real part. (3) The laser beam intensity is symmetric about the z-axis with a profile $g(r)$ normalized such that $\int_0^\infty g(r)2\pi r dr = 1$. For simplicity, we assume that the profile is Gaussian. In practice, the PA signal is insensitive to small, off-axis displacements of the beam. (4) The intensity is attenuated by absorption only along its path through the cell according to the Beer–Lambert law. Thus $I(z) = I(0)e^{-\alpha(\nu)z}$, where $\alpha(\nu)$ is the absorption coefficient at optical frequency ν for the absorbing species, and z is the distance from the window where the beam enters the cell. Scattering is neglected.

During a modulation cycle, the heat generated from an absorption event diffuses a characteristic distance equal to the thermal penetration length $\delta_T = \sqrt{2D_T/\omega}$, where D_T is the gas' thermal diffusivity. For ambient air and a modulation frequency of 1.6 kHz, $\delta_T \approx 65$ μm. By comparison, the average distance between absorption events during the cycle $d_a = [fh\nu A_L/(W_0\alpha)]^{1/3}$, which is about 2.4 μm for the measurements presented here, is much smaller than the penetration length. Therefore, we assume a continuum model for the heat generated in the gas.

With these assumptions, the amount of energy per unit volume absorbed by the gas at the point **r**, during a time interval Δt, is

$$\Delta\mathcal{E}(\mathbf{r}, t, \nu) \approx \alpha(\nu)W_0 e^{i\omega t}g(r)e^{-\alpha z}\Delta t. \tag{1}$$

The absorbed energy excites vibrational, rotational, or electronic states of the gas molecules. These excited states relax by radiative and nonradiative processes. Typically, radiative relaxation processes are not detected by PA techniques since the radiated photons will probably not be absorbed by the gas. Nonradiative relaxation by molecular collisions transfers energy from the excited state to vibrational, rotational, and translational degrees of freedom, thereby bringing the system back to equilibrium at increased temperature. The expansion of the gas, caused by the temperature rise, generates a pressure wave in the surrounding gas. If all the absorbed optical energy is converted rapidly to kinetic energy, then the local pressure p increases at the rate

$$\frac{\Delta p}{\Delta t} \approx \frac{\gamma - 1}{\beta_P T}\alpha W_0 g(r)e^{i\omega t - \alpha z}, \tag{2}$$

where $\beta_P = -(1/\rho)(\partial\rho/\partial T)_P$ is the volume expansivity and γ is the specific heat ratio.

In general, nonradiative relaxation may occur through many channels (especially in mixtures), each channel being a multistep cascade of events. In most cases, the time τ for the excited states to relax to the translational degrees of freedom is very short compared to the acoustic cycle. However, in some cases there is a bottleneck in the cascade that dramatically increases the relaxation time. When the relaxation time is larger than the acoustic period, the efficiency of acoustic wave generation is significantly reduced. We define a relaxation response function $\mathcal{R}(\omega\tau)$, which is a function of the quantity $\omega\tau$, that accounts for the reduced energy conversion when $\omega\tau \gtrsim 1$ and approaches unity for $\omega\tau \ll 1$. The rate of change of the pressure due to light absorption in the presence of relaxation is therefore

$$\frac{\partial\tilde{p}}{\partial t} \approx \frac{\gamma - 1}{\beta_P T}\alpha W_0 \mathcal{R}(\omega\tau)g(r)e^{i\omega t - \alpha z} \equiv \frac{\gamma - 1}{\beta_P T}\mathcal{H}(\mathbf{r}, \omega, t). \tag{3}$$

The acoustic pressure $\tilde{p}$ is a small pressure change about the average pressure p, and $\mathcal{H}(\mathbf{r}, \omega, t) \equiv H_\omega(\mathbf{r})e^{i\omega t}$ is the instantaneous rate that heat is deposited per unit volume in the gas. The propagation of the sound wave that results from the light absorption is described by the inhomogeneous wave equation

$$\nabla^2\tilde{p} - \frac{1}{c_s^2}\frac{\partial^2\tilde{p}}{\partial t^2} = -\frac{\gamma - 1}{\beta_P T c_s^2}\frac{\partial\mathcal{H}(\mathbf{r}, \omega, t)}{\partial t}, \tag{4}$$

where c_s is the speed of sound. (See Sec. 7.1 in Morse and Ingard.[16])

B. Molecular relaxation

A simplified model for the effect of molecular relaxation on PA sound generation assumes a two-state system characterized by a single relaxation time.[14] The molecule is in its lower energy state when the molecule is in thermal equilibrium with its surroundings. The molecule is in a higher (excited) state after absorption of a photon. We denote the num-

ber density of molecules in the equilibrium state as n and the number density of molecules in the excited state as n^*, such that the total number density $\hat{n}$ is fixed. The rate at which molecules are being excited per unit volume is $n\sigma_\nu\Phi_\nu$, where Φ_ν is the incident flux of photons (number per unit area per unit time) with optical frequency ν and σ_ν is the absorption cross section. The rate of change of the density of excited molecules is

$$\frac{dn^*}{dt} = (n - n^*)\sigma_\nu\Phi_\nu - n^*(\mathcal{A}_{rad} + \kappa_{col}), \qquad (5)$$

where $n + n^* = \hat{n}$, $\mathcal{A}_{rad}$ is the spontaneous (radiative) decay rate per excited particle (Einstein "A" coefficient), and κ_{col} is the collisional (nonradiative) decay rate per excited particle. The term $n^*\sigma_\nu\Phi_\nu$ accounts for stimulated emission. The photon flux is modulated at the acoustic frequency between zero and the maximum, i.e., $\Phi_\nu = \bar{\Phi}_\nu(1 + e^{i\omega t})$. The exact solution of Eq. (5) for n^* contains a transient term $n_0^*(t)$ and a steady-state oscillation $n_\omega^*(t)$. The transient term decays with a characteristic time τ, where $\tau^{-1} = 2\sigma_\nu\bar{\Phi}_\nu + \mathcal{A}_{rad} + \kappa_{col}$ is the sum of the excitation (pumping) rate $\tau_e^{-1} = 2\sigma_\nu\bar{\Phi}_\nu$ and the relaxation rate $\tau_r^{-1} = \mathcal{A}_{rad} + \kappa_{col}$.

When the excitation rate is low, $\sigma_\nu\tau\bar{\Phi}_\nu \ll 1$, the ground state does not deplete appreciably, i.e., $n - n^* \approx \hat{n}$, and Eq. (5) can be linearized. The steady-state oscillation in this limit is

$$n_\omega^* = \frac{\hat{n}\sigma_\nu\tau\bar{\Phi}_\nu}{1 + i\omega\tau}e^{i\omega t} + \mathrm{O}[(\sigma_\nu\tau\bar{\Phi}_\nu)^2], \qquad (6)$$

and $\tau^{-1} \approx \tau_r^{-1}$. Only collision-induced relaxation contributes to the rate with which heat is deposited per unit volume, $\kappa_{col}n_\omega^*h\nu$. We assume that any photons emitted spontaneously leave the system without being reabsorbed. Therefore the heat-generating function $H_\omega(\mathbf{r})$ is

$$H_\omega(\mathbf{r}) = \frac{\kappa_{col}\tau}{1 + i\omega\tau}\hat{n}\sigma_\nu\bar{\Phi}_\nu h\nu = \frac{\kappa_{col}\tau}{1 + i\omega\tau}\alpha W_0 g(r)e^{-\alpha z}. \qquad (7)$$

By comparison with Eq. (3), the relaxation response function is $\mathcal{R}(\omega\tau) = \kappa_{col}\tau/(1 + i\omega\tau)$. Two factors contribute to the effect of relaxation on the PA signal. First, the quantity $\kappa_{col}\tau = (1 + \mathcal{A}_{rad}/\kappa_{col})^{-1}$ is nearly unity when $\mathcal{A}_{rad} \ll \kappa_{col}$, and it gets smaller as the ratio $\mathcal{A}_{rad}/\kappa_{col}$ increases. Second, the denominator of Eq. (7) is nearly unity when the relaxation time is short compared to the acoustic period ($\omega\tau \ll 1$). As $\omega\tau$ increases, the amount of heat deposited decreases and is phase shifted with respect to the light modulation.

The relaxation model for a three-level system is a straightforward extension of the two-level model derived above. In this case, the molecule has two excited states with energies $h\nu_2 > h\nu_1$ above the ground state. The molecule is laser pumped to the higher state from which the molecule can relax back to the ground state by giving up the full energy $h\nu_2$, or it can relax to the intermediate state first, by giving up energy $h\nu_{21} = h\nu_2 - h\nu_1$, and then relaxing to the ground state by giving up energy $h\nu_1$. These transitions occur at different rates by radiation and by collisions. Three characteristic times emerge from this model: τ_{20}, the time for relaxation from state 2 directly to the ground state 0; τ_{21}, the time for relaxation from state 2 to the intermediate state 1;

and τ_{10}, the time for relaxation from state 1 to state 0. A full analysis of the relaxation of such a three-level system is beyond the scope of this article. Instead, we focus here on a special case where τ_{20} and τ_{10} are very long compared to an acoustic cycle, but τ_{21} is comparable to an acoustic cycle. In this case, only a fraction of the absorbed energy $\varepsilon \equiv \nu_{21}/\nu_2$ is released as heat during an acoustic cycle and may contribute to the PA response. In this limit, the relaxation response function is

$$\mathcal{R}(\omega\tau) = \frac{\kappa_{21}\tau_{21}\varepsilon}{1 + i\omega\tau_{21}}. \qquad (8)$$

We see that this limit is analogous to a two-level system except that only a fraction ε of the laser energy is available to generate a PA signal even when the $2 \rightarrow 1$ transition occurs efficiently ($\omega\tau_{21} \ll 1$). The importance of this result for the PA study of oxygen is discussed in the next section.

Molecular relaxation also contributes to the bulk viscosity (or second viscosity), which affects the propagation of sound regardless of the method by which the sound is generated.[16,17] Bulk viscosity is due to the temperature-dependent distribution of molecular states in thermal equilibrium. As a sound wave propagates through the medium, the local temperature oscillates due to the nearly adiabatic pressure oscillation, and the distribution of states adjusts to the temperature change. The adjustment of the distribution involves energy transfer between the kinetic and internal degrees of freedom that occurs on a time scale τ_b (different from the τ discussed above). The resultant dispersion in the speed of sound and increased acoustic energy dissipation is most prominent when $\omega\tau_b \approx 1$. In ambient air with 30% relative humidity, τ_b is about 9 μs, but even at 1.6 kHz ($\omega\tau_b \approx 0.1$), approximately 97% of the attenuation of freely propagating sound is due to molecular relaxation.[18] In an acoustic resonator, however, the attenuation is usually dominated by surface dissipation.[17,19] Bulk viscosity contributes at most 0.2% of the dissipation and changes the speed of sound by about 1×10^{-6} of the thermodynamic value in our PA resonator. We neglect the bulk viscosity for the remainder of this article and include this discussion for completeness only.

C. Driven response function

The steady-state response of the acoustic pressure due to light absorption in a closed cavity is governed by the wave equation, Eq. (4), plus the appropriate boundary condition.[16,17] Since the source is sinusoidal with time, the acoustic pressure has the form $\tilde{p}(\mathbf{r}, t) = \tilde{p}_\omega(\mathbf{r})e^{i\omega t}$, where $\tilde{p}_\omega(\mathbf{r})$ is a solution to the inhomogeneous Helmholtz equation

$$\nabla^2\tilde{p}_\omega(\mathbf{r}) + (\omega/c_s)^2\tilde{p}_\omega(\mathbf{r}) = -\frac{\gamma - 1}{c_s^2\beta_P T}i\omega H_\omega(\mathbf{r}). \qquad (9)$$

The boundary condition at $\mathbf{r}_w$ on the cavity wall specifies the normal component of $\nabla\tilde{p}_\omega$ in terms of the specific acoustic admittance at the wall $y_w(\omega, \mathbf{r}_w)$, i.e.,

$$\hat{\mathbf{n}} \cdot \nabla \widetilde{p}_\omega = -\frac{i\omega}{c_s} y_w(\omega, \mathbf{r}_w)\widetilde{p}_\omega, \tag{10}$$

where $\hat{\mathbf{n}}$ is the outward-pointing unit vector normal to the boundary. The complex-valued admittance $y_w(\omega, \mathbf{r}_w)$ includes the effect of the thermoacoustic boundary layer, which is responsible for the dominant energy loss in our acoustic resonator. When the thermal conductivity and viscosity of the gas are neglected, then y_w will be zero, since the wall is assumed to be perfectly rigid. We calculate the solution to Eq. (9) using a standard Green's function $G_\omega(\mathbf{r}|\mathbf{r}')$ expanded as a sum over the normal modes $\Psi_\mathcal{N}(\mathbf{r})$. The function $\Psi_\mathcal{N}(\mathbf{r})$ is defined as the potential for the particle velocity $\mathbf{u}_\mathcal{N} = \nabla\Psi_\mathcal{N}$, and it is proportional to the acoustic pressure $\widetilde{p}_\mathcal{N} = -i\omega\rho\Psi_\mathcal{N}$. The subscript $\mathcal{N}$ is an identifier that uniquely specifies a particular mode. Each normal mode is a solution to the homogeneous Helmholtz equation

$$\nabla^2\Psi_\mathcal{N}(\mathbf{r}) + K_\mathcal{N}^2\Psi_\mathcal{N}(\mathbf{r}) = 0, \tag{11}$$

with eigenvalue $K_\mathcal{N}$ and is subject to the same boundary condition as $\widetilde{p}_\omega$, i.e., $\hat{\mathbf{n}} \cdot \nabla\Psi_\mathcal{N} = -(i\omega/c_s)y_w(\omega, r_w)\Psi_\mathcal{N}$. $K_\mathcal{N}$ is complex valued because y_w has an imaginary part due to the boundary layer. The steady-state response at any point $\mathbf{r}$ within the cavity volume V is

$$\widetilde{p}_\omega(\mathbf{r}) = \sum_\mathcal{N} \frac{\gamma - 1}{\beta_P T}\frac{i\omega\Psi_\mathcal{N}(\mathbf{r})}{V\Lambda_\mathcal{N}(c_s^2 K_\mathcal{N}^2 - \omega^2)}\int_V H_\omega(\mathbf{r}')\Psi_\mathcal{N}(\mathbf{r}')\mathrm{d}^3r', \tag{12}$$

where $V\Lambda_\mathcal{N} = \int_V \Psi_\mathcal{N}^2 \mathrm{d}^3r$. The pressure in Eq. (12) is a sum of the response functions of all the modes. Typically, the largest terms are those for which the drive frequency is close to one of the eigenvalues $c_s K_\mathcal{N}$. The zeros of the denominator define a set of complex frequencies $F_\mathcal{N} = c_s K_\mathcal{N}/(2\pi)$, where $f_\mathcal{N} = \mathrm{Re}(F_\mathcal{N})$ is the resonance frequency of mode $\mathcal{N}$ and $g_\mathcal{N} = \mathrm{Im}(F_\mathcal{N})$ is the resonance half width. The half width is defined such that when the frequency is $f_\mathcal{N} \pm g_\mathcal{N}$, the acoustic energy drops to half of the peak value (the acoustic pressure drops to $1/\sqrt{2}$ of its peak value). The resonance quality factor $Q_\mathcal{N}$ is $f_\mathcal{N}/(2g_\mathcal{N})$.

Our PA resonator, described in the next section, has a low-order mode that couples most efficiently to the modulated laser beam and yet is isolated from other acoustic modes. We identify this special mode, the PAS mode, with the notation S1. The response measured with the microphone (at $\mathbf{r} = \mathbf{r}_m$) when f is near f_{S1} is

$$\bar{p}_\omega(\mathbf{r}_m) = \frac{\gamma - 1}{\beta_P T}\frac{i\omega\langle\Psi_{S1}(\mathbf{r}_m)\rangle_m}{V\Lambda_{S1}(c_s^2 K_{S1}^2 - \omega^2)}\int_V H_\omega(\mathbf{r}')\Psi_{S1}(\mathbf{r}')\mathrm{d}^3r'$$
$$+ \sum_{\mathcal{N}\neq S1} \mathcal{A}_\mathcal{N}(\omega)\langle\Psi_\mathcal{N}(\mathbf{r}_m)\rangle_m, \tag{13}$$

where we pulled out the PAS-mode term from the summation, and $\langle\cdots\rangle_m$ refers to an average over the microphone's sensitive area so that $\bar{p}_\omega(\mathbf{r}_m) = (1/A_{mic})\int_{A_{mic}}\widetilde{p}_\omega(\mathbf{r})\mathrm{d}A$. The remaining terms in the summation are small and contribute to the background response. Substituting $H_\omega(\mathbf{r})$ from Eq. (7), the frequency response of the PAS mode only is

$$\bar{p}_\omega(\mathbf{r}_m) = \frac{\gamma - 1}{\beta_P T}\frac{if\mathcal{R}\alpha W_0}{F_{S1}^2 - f^2}\frac{\langle\Psi_{S1}(\mathbf{r}_m)\rangle_m}{2\pi V\Lambda_{S1}}$$
$$\times \int_V g(r')e^{-\alpha z'}\Psi_{S1}(\mathbf{r}')\mathrm{d}^3r'. \tag{14}$$

When the laser modulation frequency f equals f_{S1}, Eq. (14) becomes

$$\bar{p}_{S1}(\mathbf{r}_m) \approx \frac{\gamma - 1}{\beta_P T}\frac{Q_{S1}\mathcal{G}_{S1}L}{2\pi f_{S1}V}\mathcal{R}_{S1}\alpha W_0, \tag{15}$$

where L and V are the resonator's total length and volume, respectively. Here we approximate $1 + i/(4Q_{S1}) \approx 1$ in the denominator, we define $\mathcal{R}_{S1} = \mathcal{R}(f_{S1})$, and we define the dimensionless overlap integral $\mathcal{G}_{S1}$ as

$$\mathcal{G}_{S1} = \langle\Psi_{S1}(\mathbf{r}_m)\rangle_m\frac{\dfrac{1}{L}\displaystyle\int_V g(r')e^{-\alpha z'}\Psi_{S1}(\mathbf{r}')\mathrm{d}^3r'}{\dfrac{1}{V}\displaystyle\int_V [\Psi_{S1}(\mathbf{r}')]^2\mathrm{d}^3r'}. \tag{16}$$

Finally, we define the cell constant C_{S1} as

$$C_{S1} = \frac{\bar{p}_{S1}(\mathbf{r}_m)}{\mathcal{R}_{S1}\alpha W_0} \approx \frac{\gamma - 1}{\beta_P T}\frac{Q_{S1}\mathcal{G}_{S1}L}{2\pi f_{S1}V}, \tag{17}$$

which depends on the properties of the gas medium through the heat capacity ratio γ, the isobaric thermal expansivity β_P, the speed of sound (through f_{S1}), and the transport properties (through Q_{S1}). The cell constant does not depend strongly on the laser wavelength. The cell constant C_{S2} for the S2 mode (discussed in Sec. III) is similarly defined. Note that the acoustic pressure in Eqs. (9)–(17) is the zero-to-peak amplitude if W_0 is the zero-to-peak amplitude of the bipolar power (half of the peak-to-peak power). If the root-mean-squared (rms) pressure amplitude is used in Eq. (17), e.g., as measured with a lock-in amplifier, then the laser power must also be the rms value.

The first equality in Eq. (17) shows that one can measure C_{S1} using a calibrated microphone and a calibrated optical power meter, provided that α and $\mathcal{R}_{S1}$ are known.[1,5] The second equality in Eq. (17) shows that one can determine C_{S1} from measurements of the resonance frequency and quality factor, without the need for a calibrated microphone or a calibrated power meter, provided that γ and β_P are known and that one can calculate the geometric factor $\mathcal{G}_{S1}L/V$ with sufficient accuracy. Only by comparing C_{S1} from both methods can we get a true estimate of the uncertainty. If $\mathcal{R}_{S1}$ is unknown *a priori*, which is usually the case, then a check on the cell constant is imperative.

III. EXPERIMENTAL DESIGN

Our resonator design had some similarities with resonators used in other laboratories.[20] The resonator design, shown schematically in Fig. 1, consisted of a central duct, 100 mm long and 6 mm in diameter, positioned between two chambers that were 50 mm long and 30 mm in diameter. An optical window (with antireflection coating on both flat surfaces) was mounted axially in the wall of each chamber. The
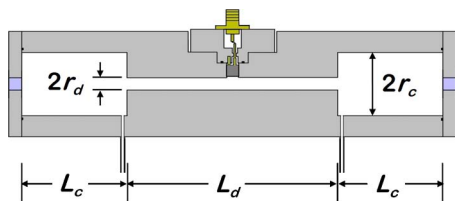
FIG. 1. (Color online) Schematic of the PA resonator used in this work with nominal dimensions $L_d=100$ mm, $2r_d=6$ mm, $L_c=50$ mm, and $2r_c=30$ mm.

FIG. 2. Measured sensitivity of Knowles (MD6052USZ-1) electret microphone under ambient conditions (RH$\approx 40\%$). Calibration was performed against a calibrated Brüel and Kjær, type 4138, 1/8 in. condenser microphone in an acoustic coupler with a Brüel and Kjær, type 4136, 1/4 in. condenser microphone cartridge as a frequency-doubling source.

resonator was made from brass with leak-tight, indium-wire seals. We used an electret microphone (Knowles, MD6052USZ-1) (Ref. [21]) as a sound detector located midway between the ends of the duct. Two small tubes (1.6 mm inner diameter) were used to flow gas into and out of the resonator. One tube was attached in each chamber close to the junction with the central duct. These junctions are near acoustic pressure nodes, and at these locations the effect of the tube's admittance on the resonator's frequency response is minimal. Furthermore, under steady flow conditions, the incoming gas mixes thoroughly with the gas in the chamber because the flow velocity of the entering gas is 14 times higher than the velocity in the main duct.

We chose the design in Fig. 1 based on the following considerations: (1) the mode used for PAS (the PAS mode) is nondegenerate and isolated from other modes, (2) the PAS mode couples efficiently to the modulated laser intensity, (3) the microphone signal is insensitive to synchronous optical absorption by the windows, (4) the resonator response is insensitive to the acoustic impedance of the gas-flow plumbing, and (5) the microphone has low noise and a smooth frequency response.

The central duct (length L_d) behaves nearly as a half-wave resonator with open ends. Below the cutoff frequency for transverse modes, only nondegenerate plane-wave modes exist. The longitudinal normal modes of an open-ended, half-wave resonator occur when an integer number ℓ of acoustic half-wavelengths fit between the pressure nodes at the open ends, i.e., $\ell\lambda/2=L_d$. The longitudinal modes for which ℓ is odd have a pressure antinode at the duct's midpoint, and they are symmetric about the plane that bisects the duct's length. The longitudinal modes for which ℓ is even have a pressure node at the duct's midpoint, and they are antisymmetric about the midplane. The antisymmetric modes do not couple efficiently to an axial laser excitation because the overlap integral in Eq. (16) contains equal positive and negative phases of the wave function that cancel out, and the integral vanishes. On the other hand, the overlap integral for the symmetric modes (odd ℓ) does not vanish, but it decreases as $1/\ell$. The lowest-order symmetric mode ($\ell=1$), which we designate as S1, has the largest overlap integral and, therefore, the most efficient coupling to the laser excitation. The S1 mode was used for the PAS measurements. The second symmetric mode S2, with $\ell=3$, has less efficient coupling than S1 by a factor of 3. The S2 mode was used to study the frequency-dependent molecular relaxation effects discussed in Sec. II. We refer to the S1 and S2 modes as the PAS modes.
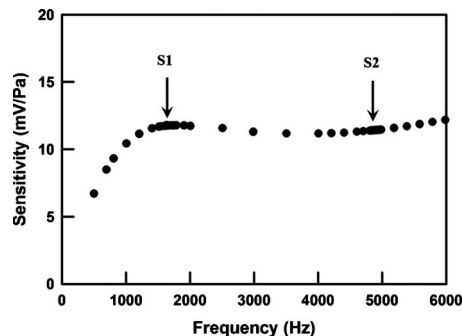
The resonance frequencies are perturbed from that of an open-ended, half-wave resonator by an amount proportional to $A_d/A_c\approx 0.04$, where A_d is the cross-sectional area of the duct and A_c is the cross-sectional area of the chamber. Due to their low acoustic impedances, the chambers at either end of the central duct act as buffers that reduce the background signal from absorption by the windows, and they reduce the perturbation from the inlet and outlet ports. We estimate that the ports change the measured acoustic pressure of the S1 mode by less than $55\times 10^{-6}\bar{p}_{S1}$ and change its resonance frequency by less than $1\times 10^{-6}f_{S1}$.

We calibrated the electret microphone sensitivity under ambient conditions against a Brüel and Kjær (B & K), type 4138, 1/8 in. condenser microphone.[21] We checked the calibration of the condenser microphone against a B & K, type 4228 pistonphone. Both the electret and the condenser microphones were mounted in a small acoustic coupler with a B & K, type 4136, 1/4 in. microphone cartridge used as a frequency-doubling sound source.[22] We measured the sensitivity of the electret microphone under similar conditions of temperature, pressure, and relative humidity (RH$\approx 40\%$) for which the O_2 A-band measurements were obtained. The calibration is shown in Fig. 2. We also measured the dependence of the microphone sensitivity on RH. Under the conditions of the CO_2 measurements (RH=28%), reported below, the microphone sensitivity was 1.3% below the calibration in Fig. 2.

We measured the acoustic response of the PA cell with one window replaced by a sound source. The sound source consisted of a piezoceramic disk [lead zirconate titanate (PZT)] attached to a diaphragm that was mounted in the endplate flange. A radial strain developed within the PZT disk in response to an applied voltage from a function generator (Stanford Research, DS345) and caused the diaphragm to bend. A dual-phase lock-in amplifier (Stanford Research Systems, model SR830) measured the synchronous output signal from the microphone. At each frequency, we recorded the in-phase component u and the quadrature component v of the microphone signal referenced to the function generator. Figure 3 shows the absolute magnitude of the measured acoustic spectrum up to 5 kHz when the cell was filled with ambient air. The S1 and S2 modes are obviously well iso-
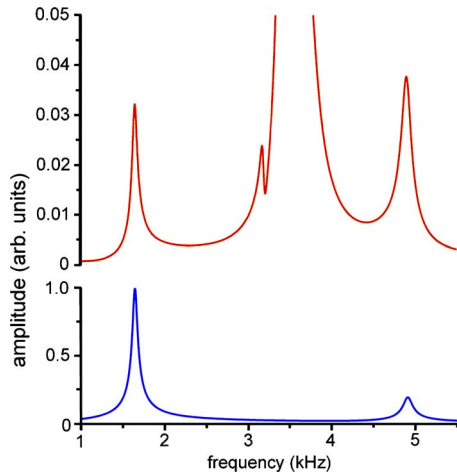
FIG. 3. (Color online) Top panel: measured response of PA cell to excitation by a PZT source. Bottom panel: measured response to laser excitation, showing the S1 and S2 PAS modes near 1.6 and 4.8 kHz, respectively. The laser excitation does not efficiently couple to the modes between 3 and 4 kHz.
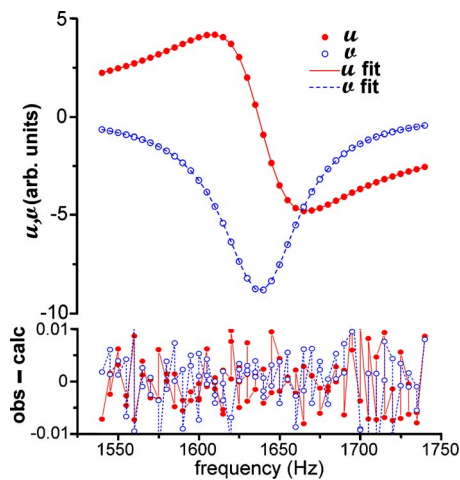

FIG. 4. (Color online) Measured acoustic resonance (S1 PAS mode) and fit to complex resonance function corresponding to laboratory air at $T = 300$ K and $p = 98.5$ kPa. The PA cell excitation was by the PZT source. Fitted values include $f_0 = 1638.22$ Hz and $g = 29.2$ Hz. Upper panel: α and α' measurements (symbols) and fits (lines). Bottom panel: fit residuals for α and α' components.

lated from other modes. The measured PA spectrum is also shown in Fig. 3. The insensitivity of the PA signal to the antisymmetric mode around 3600 Hz compared to the signal from the PZT source is striking.

The data in the vicinity of each mode ($f_r - 2g \leq f \leq f_r + 2g$) were fit with the resonance response function[22] based on Eq. (14),

$$\alpha + i\alpha' = \frac{if\mathcal{A}}{(f_r + ig)^2 - f^2} + \mathcal{B} + \mathcal{C}(f - \bar{f}). \qquad (18)$$

The resonance frequency f_r, the half width g, the complex amplitude $\mathcal{A}$, and the complex background parameters $\mathcal{B}$ and $\mathcal{C}$ were adjusted parameters. The background terms are present to account for the tails of other modes, frequency dependence of the transducers, cross talk, etc. The linear background term was included only if it was justified by an F test at the 95% level. The parameter $\bar{f}$ was not adjusted but was defined as the midpoint between the lowest and highest frequency in the data set. Figure 4 shows an example of the measured response of the S1 mode in air at 100 kPa and the deviations from the eight-parameter fit. The resonance frequencies and half widths in air and in nitrogen were measured with this technique as a function of pressure between 17 and 100 kPa. The quantity $|\mathcal{V}_{max}|/\sigma_\mathcal{V}$ is the signal-to-noise ratio, where $|\mathcal{V}_{max}|$ is the absolute magnitude of the signal at resonance and $\sigma_\mathcal{V}$ is the rms deviation from the fit, ranged from 160 at 17 kPa to 2000 at 100 kPa. A summary of the gas properties[23] is given in Table I.

The acoustic model for our PA resonator, shown schematically in Fig. 5, is a lumped-element acoustic circuit.[24–26] The model contains elements for the main duct, the chambers, the junction between the chambers and the duct (end effects), and the microphone. The elements include the effects of dissipation from thermal and viscous boundary layers adjacent to the wall. We model the chambers and the main duct as lossy transmission lines, represented by T networks in the circuit diagram. The elements of the T network account for the viscous and thermal dissipation at the wall of a circular duct in terms of a complex propagation constant Γ_x and a characteristic impedance Z_{0x}, where x is either "c" or "d" for the chamber or duct, respectively. In each chamber, the thermal boundary layers on the endplate and on the opposite wall at the junction with the main duct are modeled as acoustic admittances $Y_P = 1/Z_P$ and $Y'_P = 1/Z'_P$, respectively.[17] Additional inertial and dissipative effects due to the diver-

TABLE I. Gas properties at 300 K and 0.101 325 MPa pressure from Ref. 23.

Gas	M (kg mol^{-1})	ρ (kg m^{-3})	γ	$\beta_P T$	c_s (m s^{-1})	D_t (m^2 s^{-1})	Pr
N$_2$	28.013	1.1381	1.4012	1.0025	353.16	2.1910×10^{-5}	0.7174
O$_2$	31.999	1.3007	1.3965	1.0032	329.72	2.2136×10^{-5}	0.7173
Dry air[a]	28.966	1.1770	1.4017	1.0027	347.32	2.1936×10^{-5}	0.7196
Wet air[b]	28.856	1.1726	1.4009	1.0028	347.86	2.1900×10^{-5}	0.7235

[a]The molar compositions of dry air are defined as N$_2$ (0.780 84), O$_2$ (0.209 46), Ar (0.009 34), and CO$_2$ (383 ppm).
[b]Wet air is defined as dry air with 1% H$_2$O. The molar compositions of wet air are assumed to be N$_2$ (0.773 03), O$_2$ (0.207 36), Ar (0.009 246), CO$_2$ (379 ppm), H$_2$O (0.01). D_v and D_t were estimated assuming that the viscosity and thermal conductivity are the same as dry air.
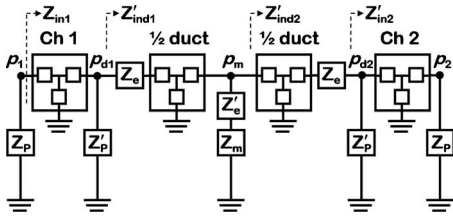
FIG. 5. Lumped-element acoustic circuit for the resonator shown in Fig. 1. The chambers and the duct are acoustic transmission lines modeled by T networks. The duct is split in half by the microphone impedance Z_m. The nonideal flow and added dissipation due to the finite-length duct are included in the impedance Z_e at each end of the duct. The effective compliance of the thermal boundary layer at the endplates of the chambers is included in the impedances Z_P and Z_P'.

gent flow at the ends of the duct are included in the impedance Z_e, which is responsible for the familiar effective length correction.[27] The impedance of the microphone Z_m is represented by an inertance (due to the orifice opening), a compliance (due to the effective volume), and a resistance (due to internal energy losses). This model was used to estimate the resonance frequencies and half widths. Comparisons of the measured and estimated resonance frequencies and quality factors for air and dry nitrogen are shown in Fig. 6.

We approximate the integrals in Eq. (16) using the velocity potential in the limit of no boundary layer. We estimate using perturbation theory that the coefficient of the leading fractional correction in Eq. (16) due to the boundary layer is of order 1×10^{-5} for our resonator.[16] The velocity potential for the PAS modes in this limit has the form $\varphi(z) = B \cos(kz + \phi)$ in each of the resonator's four sections (two chambers and two half ducts),

$$\varphi_c(z) = B_c \cos\left[k\left(|z| - \tfrac{1}{2}L_d - L_c\right)\right],$$

$$\tfrac{1}{2}L_d \le |z| \le \tfrac{1}{2}L_d + L_c, \tag{19a}$$

$$\varphi_d(z) = B_d \cos(k|z| + \phi), \quad 0 \le |z| \le \tfrac{1}{2}L_d. \tag{19b}$$

The boundary conditions on $\varphi(z)$ are

$$\frac{d\varphi_c}{dz} = 0 \quad \text{at} \quad z = \pm\frac{1}{2}L_d \pm L_c, \tag{20a}$$

$$\frac{-i\omega\rho\varphi_c}{A_c d\varphi_c/dz} - \frac{-i\omega\rho\varphi_d}{A_d d\varphi_d/dz} = \mp Z_e \quad \text{at} \quad z = \pm\frac{1}{2}L_d, \tag{20b}$$

$$\frac{d\varphi_d}{dz} = \frac{\rho\omega\varphi_d}{2iA_d Z_m} \quad \text{at} \quad z = 0, \tag{20c}$$

where $Z_e = i\rho\omega\delta_l/A_d$ (neglecting dissipation) and δ_l is the inertial length correction.[25–27] The velocity potential defined by Eq. (19) is consistent with the boundary conditions if the parameters k, ϕ, B_c, and B_d satisfy the relationships

$$\tan(\phi) = \frac{\rho c}{2iA_d Z_m}, \tag{21a}$$

$$\frac{A_d}{A_c}\cot(kL_c) + \cot\left(\frac{1}{2}kL_d + \phi\right) = k\delta_l, \tag{21b}$$
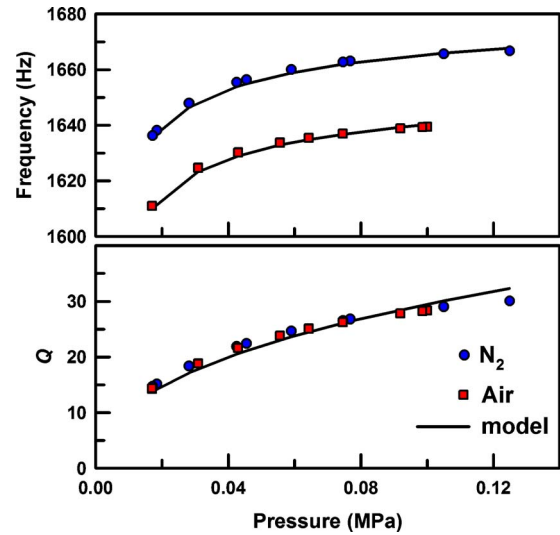

FIG. 6. (Color online) Measured and modeled resonance frequencies (top) and quality factors Q (bottom) of the S1 mode when the resonator was filled with nitrogen or air at 300 K as a function of pressure.

$$\frac{B_c}{B_d} = -\frac{A_d \sin\left(\frac{1}{2}kL_d + \phi\right)}{A_c \sin(kL_c)}. \tag{21c}$$

We evaluated the integrals in Eq. (16) analytically to obtain

$$\frac{L}{V}\mathcal{G}_{S1} \approx (4.161 \pm 0.009) \times 10^4 \text{ m}^{-2}. \tag{22}$$

The uncertainty given in Eq. (22) is dominated by the uncertainty of microphone impedance ($\sim 0.2\%$) and the uncertainty of the inertial length correction ($\sim 0.1\%$).

IV. SPECTROSCOPY OF THE O$_2$ A-BAND

The O$_2$ A-band, centered at wave number $\tilde{\nu} = 13\,122$ cm^{-1}, contains transitions within the $b\,^1\Sigma_g^+ \leftarrow X\,^3\Sigma_g^-(0 \leftarrow 0)$ band of molecular oxygen.[10,11] This band plays an important role in near-infrared absorption in the earth's atmosphere, and it is widely used for ground-based and satellite-based[28–30] measurements of atmospheric gases. Here we consider the relatively weak and spectrally isolated ^{16}O$_2$ magnetic-dipole A-band transitions. These have line intensities of the order 10^{-23} cm molecule^{-1} and are $\sim 10^7$ times weaker than typical near-infrared electric dipole transitions. Given the importance of the O$_2$ A-band to atmospheric science and remote sensing, its line parameters (positions, intensities, and line shape coefficients) have been extensively measured. Updated O$_2$ A-band line parameters are archived in the 2008 version of the HITRAN (high-resolution transmission) molecular spectroscopic database.[9] Importantly, these line intensities have relative uncertainties $<0.5\%$,[10] making them attractive as reference values for the present study. Table II summarizes the O$_2$ A-band lines that we probed. The A-band transitions are described by $^{\Delta N}\Delta J(N'')$, where N is the rotational angular momentum, J is the total angular momentum, and the double prime indicates the lower state. We use the standard spectroscopic notation P and Q to indicate ΔN or $\Delta J = -1$ and 0, respectively.

TABLE II. Line parameters for the $^{16}O_2$ transitions probed in this study: zero-pressure wave number $\tilde{\nu}_0$, lower state energy E'', FWHM Doppler width $\delta\nu_D$ ($T_r = 296$ K), reference line intensity S_{HT} ($T_r = 296$ K), line broadening, and narrowing coefficients γ_{air}, γ_{self}, and γ_{nar}. The parameter n_γ is the dimensionless temperature exponent. Broadening coefficients and narrowing coefficients are taken from Havey *et al.* (Ref. 10) and Robichaud *et al.* (Ref. 11), respectively. All other data are from HITRAN 2008 (Ref. 9).

Transition	$\tilde{\nu}_0$ (cm^{-1})	E''/hc (cm^{-1})	S_{HT} (cm molecule^{-1})	$\delta\nu_D$ (GHz)	γ_{air} (MHz Pa^{-1})	γ_{nar} (MHz Pa^{-1})	n_γ (10^{-3})
$^PP(9)$	13 091.7104	130.4375	8.298×10^{-24}	0.854 95	0.0146	0.0030	0.74
$^PQ(9)$	13 093.6558	128.4921	7.276×10^{-24}	0.855 08	0.0146	0.0030	0.74
$^PP(11)$	13 084.2035	190.7748	7.435×10^{-24}	0.854 46	0.0141	0.0038	0.72
$^PQ(11)$	13 086.1252	188.8531	6.683×10^{-24}	0.854 59	0.0141	0.0024	0.73

V. DESCRIPTION OF EXPERIMENT, ANALYSIS METHOD, AND BACKGROUND

A. Experimental method

The principal elements of the PA spectrometer system are depicted in Fig. 7 and consist of a light source, intensity modulator, wavelength meter, PA cell, power meter, two-channel phase-sensitive (lock-in) amplifier, and data acquisition system (not shown). The light source was an external-cavity diode laser (ECDL) which emits up to 10 mW in the wavelength range of 759–770 nm and which provides a single-mode laser beam (<1 MHz short-term linewidth) with mode-hop-free tuning over the entire wavelength range. Fine tuning of the ECDL was actuated by an external computer using a piezoelectric-actuated mirror (full range of 60 GHz). We measured the laser wave number with a Michelson-interferometer wavelength meter [$u(\nu) = 60$ MHz]. To couple the absorbed laser power into acoustic resonances, we intensity modulated the laser beam using an acousto-optic modulator (AOM) and directed the first-order diffracted beam (~ 2.5 mW peak to peak) to the PA cell. The AOM driver operated at a carrier frequency of 80 MHz and was amplitude modulated at frequency f_{mod} using a function generator. Fourier analysis of the modulated laser intensity revealed that the AOM provided a near-perfect ($<0.3\%$ deviation) sinusoidal waveform at f_{mod} with constant efficiency over the frequency range of interest. Unlike PA current-modulation schemes that use distributed feedback lasers, our AOM introduces no residual wavelength modulation of the source laser.[31] The lock-in amplifier, which was referenced to f_{mod}, provided both in-phase and out-of-phase signals with time constant set to 10 ms.
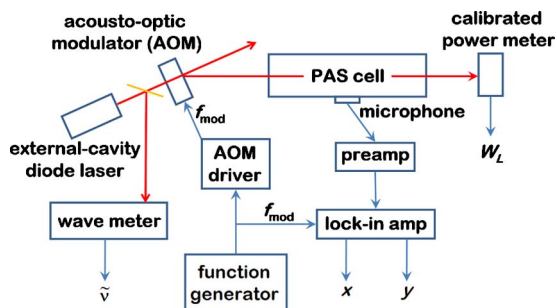
A NIST-traceable calibrated power meter measured the beam power exiting the PA cell. Spectra were recorded by step scanning the laser and then sampling the wavelength meter, lock-in amplifier outputs, and power meter. To compensate for the finite frequency response of the power meter (low-pass cutoff < 50 Hz), the peak-to-peak beam power at the beginning of each scan was measured with f_{mod} set at 10 Hz. This beam power measurement provided an absolute scaling factor for subsequent power measurements taken at higher modulation frequencies. The lock-in amplifier and power meter analog outputs were recorded using a multichannel 18-bit digitizer at 10^5 samples s^{-1}. Typically, each measurement corresponded to an average of 10^4 samples, enabling an ensemble of k values to be obtained every 0.1 s. At each wave number step of the laser, k values of the observed quantities were averaged. We found the optimal averaging time (~ 100 s) by evaluating the Allan variance[32] of the PA signal. Based on the minimum Allan variance and the system constant discussed below, we estimate a detection limit (i.e., product of peak-to-peak beam power and minimum absorption coefficient) of $\sim 4 \times 10^{-10}$ W cm^{-1} for the present system.

We measured the sample pressure using a capacitance diaphragm gauge, and we used a thermistor mounted in the PA cell wall for monitoring sample temperature. A multimeter in four-wire mode measured the thermistor resistance. The respective standard uncertainties for pressure and temperature are <100 Pa and <0.1 K. No effort was made to actively regulate the cell temperature (nominally 300 K), which exhibited diurnal variations typically less than 0.3 K. In the case of atmospheric air samples, we measured the RH to calculate the O_2 molar fraction assuming a dry gas O_2 molar fraction equal to 20.947%.

We also investigated streams of humidified, synthetic air (volumetric flow rate ~ 0.3 l min^{-1}) to quantify the effect of water on PA relaxation from the excited electronic state of O_2. The dry O_2 from a cylinder was humidified using a dynamic dilution method whereby a dry gas stream was mixed with a second stream that had passed through an isothermal bath of liquid water. We measured the humidity content at the output of the PAS chamber with a chilled-mirror hygrometer having a temperature resolution of 0.1 K. This configuration yielded atmospheric-pressure sample air streams with RH in the range of 2%–90%.

FIG. 7. (Color online) Principal components of the experimental system.

B. Spectrum analysis and data reduction

For an isolated O_2 line of intensity S centered at frequency ν_0, the absorption coefficient can be written as

$$\alpha(\nu) = ncS(T)f(\nu - \nu_0), \tag{23}$$

where c is the speed of light and ν is the optical frequency of the probe laser. The O_2 number density $n = x_{O_2}p/(k_bT)$, where k_b is the Boltzmann constant and x_{O_2} is the molar fraction of O_2. The line shape function $f(\nu - \nu_0)$ is normalized such that $\int_{-\infty}^{\infty} f(\nu - \nu_0)d(\nu - \nu_0) = 1$. We determined the PA cell constant by least-squares fits of the following model to the measured spectra:

$$\frac{[(\mathscr{u}(\nu) - \mathscr{u}_0)^2 + (\mathscr{v}(\nu) - \mathscr{v}_0)^2]^{1/2}}{W_L(\nu)} = \mathcal{K}_{\mathcal{N}}[nS(T)f(\nu - \nu_0) + \alpha_b], \tag{24}$$

where $\mathcal{K}_{\mathcal{N}} = C_{\mathcal{N}}\beta_m\mathcal{R}_{\mathcal{N}}/\sqrt{8}$ is the system constant, β_m is the microphone sensitivity, and $\mathcal{R}_{\mathcal{N}}$ is the relaxation response function from Eq. (8) that accounts for energy relaxation effects of O_2 in air (discussed below). All quantities on the left hand side of Eq. (24) were measured values that depended on laser frequency. Here, $W_L(\nu)$ is the peak-to-peak beam power at the center of the PAS cell, $\mathscr{u}(\nu)$ and $\mathscr{v}(\nu)$ are the in-phase and out-of-phase lock-in amplifier rms output voltages, respectively, and $\mathscr{u}_0$ and $\mathscr{v}_0$ represent the nonzero offsets of these channels measured when $W_L = 0$. The factor $\sqrt{8}$ in the definition of $\mathcal{K}_{\mathcal{N}}$ converts peak-to-peak power to rms power. To obtain $W_L(\nu)$, we corrected the calibrated power meter reading $W_{L,m}(\nu)$ using $W_{L,m}/W_L = \mathcal{T}^{-1}e^{-\alpha_1(\nu)\ell_1}e^{-\alpha_2(\nu)\ell_2}$, where $\mathcal{T} = 0.9866$ is the window transmittance measured at the laser wavelength, $\alpha_i(\nu)$ is the absorption coefficient in the cell ($i=1$) or in the ambient air ($i=2$), and ℓ_i is the corresponding path length. With all line-shape parameters constrained (as described below), there remained three fitted parameters: $\mathcal{K}_{\mathcal{N}}$, ν_0, and α_b. The last parameter was a linear baseline that accounted for absorption by the wings of distant lines.

We used a Galatry profile[33,34] for $f(\nu - \nu_0)$, which is completely specified by three parameters, $\delta\nu_D$, $\delta\nu_L$, and $\delta\nu_{nar}$, that correspond to the Doppler width, Lorentzian width, and narrowing frequency, respectively. We calculated the Doppler full width at half maximum (FWHM) in terms of T, ν_0, and O_2 molecular mass. The Lorentzian widths $\delta\nu_L$ were evaluated based on published pressure-broadening coefficients and temperature corrected as specified in HITRAN,[9] and $\delta\nu_{nar}$ was taken from Ref. 10 for self-broadened and air-broadened O_2. The line intensities $S(T)$ were also temperature corrected with respect to $S(T=296$ K$)$ using the lower state energy for each transition and total-internal partition function for $^{16}O_2$. All line parameters used in this study are given in Table II.

C. Electronic-to-vibrational relaxation of the O_2 A-band

The sensitivity of PA signal strength to gas mixture composition is well established, and in particular trace quantities of water vapor effectively have been shown to promote various modes of energy transfer between the absorbing gas and
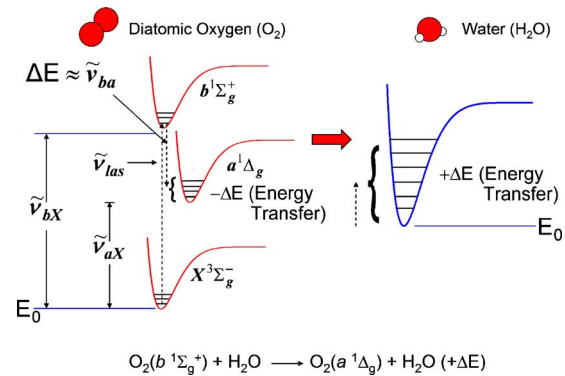

FIG. 8. (Color online) Schematic energy level diagram showing the three lowest electronic states of O_2 (left side) and ground electronic state of H_2O (right side). Energy transfer between the laser-excited O_2 (b-state) and H_2O ($v=0$) occurs upon collision. This causes O_2 relaxation to a distribution of rotation-vibration energies within its a-state and H_2O excitation to a range of rotation-vibration energies within its ground electronic state. The minima of the excited electronic states are at wave numbers $\tilde{\nu}_{aX} = 7888$ cm^{-1} and $\tilde{\nu}_{bX} = 13\,122$ cm^{-1}.

quenching partners.[6] This issue is especially important in the present study since the O_2 A-band corresponds to optical excitation of a relatively long-lived electronic state. Thus electronic-to-vibrational (E-V) and vibrational-to-vibrational (V-V) energy transfer pathways must be considered in the present experiment. To this end, we model the energy transfer dynamics and present measurements of PA signal efficiency as a function of water vapor concentration for O_2 A-band spectra.

There are three low lying electronic states of the $^{16}O_2$ molecule: the ground state $^3\Sigma_g^-$, the first excited state $^1\Delta_g$, and the second excited state $^1\Sigma_g^+$ denoted by X, a, and b, respectively.[35] As shown in Fig. 8, the minima of the two excited electronic states are located at wave numbers (relative to the ground state) $\tilde{\nu}_{aX} = 7888$ cm^{-1} and $\tilde{\nu}_{bX} = 13122$ cm^{-1}, where the latter quantity is nominally equal to the wave number of the optical transitions probed here. The $b(v=0)$ and $a(v=0)$ states are separated by a wave number (energy) difference of $\tilde{\nu}_{ba} = 5234$ cm^{-1}. Note that this quantity is $\sim 0.4\tilde{\nu}_{bX}$, where $hc\tilde{\nu}_{bX}$ is nearly equal to the energy per photon of absorbed laser power. Radiative transitions between all of these states are highly forbidden because of quantum-mechanical selection rules and have spontaneous emission rates (Einstein "A" coefficients) given by $\mathcal{A}_{bX} = 11.3$ s^{-1},[36] $\mathcal{A}_{ba} = 1.20 \times 10^{-3}$ s^{-1},[37] and $\mathcal{A}_{aX} = 2.31 \times 10^{-4}$ s^{-1}.[38]

We refer again to Fig. 8 for a schematic representation of energy transfer between the excited state O_2 and ground state H_2O. We assume that probabilities of collisional relaxation from $b \leftarrow X$ and $a \leftarrow X$ are negligible because the transitions are strongly spin forbidden and because energy gaps are large compared to $b \leftarrow a$ transitions.[39] Indeed, measured rate constants for collisional relaxation of $O_2(b\ ^1\Sigma_g^+)$ are typically one to six orders of magnitude larger than those of $O_2(a\ ^1\Delta_g)$ for a large number of collision partners.[40,41] For $O_2(b\ ^1\Sigma_g^+)$, quenching can be relatively fast with rates that vary by orders of magnitude for various collision partners including $O_2(X\ ^3\Sigma_g^-)$, N_2, CO_2, and H_2O. For the components of air, the ratios $(\kappa_{ba,i} + \kappa_{bX,i})/\kappa_{aX,i}$ are 24 for O_2, 2×10^5 for N_2,

TABLE III. Measured system constants $\mathcal{K}_{S1}$ based on Galatry fits to measured $^{16}O_2$ spectra. The sample gas was laboratory air at $p=100.7$ kPa, $T=300$ K, and RH=40%. The quantities, $\delta\nu_{L,fit}$ and $\delta\nu_{L,exp}$, are the fitted and expected Lorentzian widths (GHz), respectively. The calculated peak absorption coefficient α_0 is based on $p=101.325$ kPa and $T=296$ K. $\mathcal{K}_{S1}$ is based on peak-to-peak power.

Transition	No. of fitted spectra	$\mathcal{K}_{S1}$ (V cm W^{-1})	$\delta\nu_{L,fit}$ (GHz)	$\delta\nu_{L,exp}$ (GHz)	α_0 (cm^{-1})	Input data
$^P P(9)$	25	7.487	2.924	2.966	2.68×10^{-4}	Single scan
$^P Q(9)$	1	7.483	2.947	2.969	2.35×10^{-4}	Average of four scans
$^P P(11)$	1	7.492	2.839	2.867	2.46×10^{-4}	Average of four scans
$^P Q(11)$	1	7.461	2.849	2.868	2.21×10^{-4}	Average of four scans

2×10^7 for CO_2, and 1.2×10^6 for H_2O, where i indicates the rate associated with the ith collision partner. Of these, the most efficient quenching agent is water vapor. The reaction $O_2(b\,^1\Sigma_g^+)+H_2O\rightarrow O_2+H_2O$ has a rate constant of 5.9×10^{-12} cm^3 molecule^{-1} s^{-1}.[42] For dry and wet air, the ratios of the combined rates $(\kappa_{ba}+\kappa_{bX})/\kappa_{aX}$ are 5×10^3 (RH=0%) and 1.6×10^5 (RH=40%). If we assume that κ_{bX} is at most the same order of magnitude as κ_{aX}, then $\kappa_{ba}/\kappa_{aX}\gg1$. Therefore, the $O_2(a\,^1\Delta_g)$ state is a bottleneck.

Based on the rate constants from Ref. 42 and discussion above, we estimate $(\mathcal{A}_{bX}+\mathcal{A}_{ba})/\kappa_{ba}\ll2\times10^{-4}$ for wet or dry air. If in Eq. (8), we assign $\kappa_{21}=\kappa_{ba}$ and $\tau_{ba}=\tau_{21}$, then $\kappa_{ba}\tau_{ba}$ is very nearly unity, and thus $\tau_{ba}\approx1/\kappa_{ba}$. We have shown that the only important relaxation rate influencing the excited state population of O_2 in our experiment corresponds to water-vapor-mediated relaxation from $O_2(b\,^1\Sigma_g^+)$ to $O_2(a\,^1\Delta_g)$. We specify a single rate constant κ_{PA} that represents an average for all the energy-transfer pathways that lead to the PA signal. Since the relaxation rates to the ground state are negligible, we treat the energy transfer effectively as a two-level system with an energy difference $hc\tilde{\nu}_{ba}$ and an efficiency ε as in Eq. (8). In this limiting case, the remainder of the absorbed laser energy becomes trapped in the a-state because the lifetime of this state is long compared to the period of the acoustic cycle. As a consequence, at most only a fraction $\varepsilon=\tilde{\nu}_{ba}/\tilde{\nu}_{bX}\approx0.399$ of the absorbed laser energy contributes to the PA signal.

The definition of ε developed above assumes that the photon energy is $hc\tilde{\nu}_{bX}$. In reality the photon energy $hc\tilde{\nu}_{las}$ depends on the specific transition being probed. To take this into account, we assume that the energy cascade is a three-step process: (1) rapid thermalization of the rotational energy in the b-state, (2) slow collisional relaxation to v=0 of the a-state, and then (3) rapid thermalization of the rotational energy in the a-state. In the fully quenched limit, all of these rates are fast compared to the acoustic cycle. The absorbed energy that contributes to the PA signal is

$$E_{PA}=n^*hc\tilde{\nu}_{las}-(E_f-E_i),\qquad(25)$$

where $E_i=n\langle E_X\rangle$ is the initial energy of O_2 in the ground state and $\langle E_X\rangle$ is the average thermal energy above the $X\,^3\Sigma_g^-$(v=0) state. E_f is the sum of the energy of the nonexcited (ground state) O_2 and the energy of the O_2 a-state after the three-step cascade,

$$E_f=(n-n^*)\langle E_X\rangle+n^*[\langle E_a\rangle+hc\tilde{\nu}_{aX}],\qquad(26)$$

where $\langle E_a\rangle$ is the average thermal energy above the $a\,^1\Delta_g$(v=0) state. Since the thermalization of the rotational energies is rapid and complete, we make the further assumption that $\langle E_a\rangle=\langle E_X\rangle$. If we define the efficiency as

$$\varepsilon=\frac{E_{PA}}{n^*hc\tilde{\nu}_{las}}=\frac{\tilde{\nu}_{las}-\tilde{\nu}_{aX}}{\tilde{\nu}_{las}},\qquad(27)$$

then ε is approximately $\tilde{\nu}_{ba}/\tilde{\nu}_{bX}$ when $\tilde{\nu}_{las}\approx\tilde{\nu}_{bX}$. For the transitions probed here (see Table II), ε, given by Eq. (27), is within 0.5% of 0.399. We note that for very high-J transitions, the value of ε can change substantially [e.g., for $^PQ(61)$, $\varepsilon\approx0.383$].

VI. EXPERIMENTAL RESULTS

A. Measurements on laboratory air

We probed static samples of laboratory air at atmospheric pressure, temperature, and relative humidity conditions (RH≈40%) to measure $\mathcal{K}_{S1}$ for the S1 PAS mode. The results are given in Table III. We scanned over the $^PP(9)$ $^{16}O_2$ transition 25 times, obtaining a mean value of $\mathcal{K}_{S1}=7.487$ V cm W^{-1} with a relative standard deviation of 0.77%. Four spectra were averaged for each of the remaining three transitions, with each average yielding an independent measurement of $\mathcal{K}_{S1}$. Taken together, the deviations among the four $\mathcal{K}_{S1}$ values are less than 0.2%. Although this spread is nearly a factor of 4 smaller than the observed distribution width for those based solely on the $^PP(9)$ transition, it may not be statistically significant. Nevertheless, the inconsistency among the independent determinations of $\mathcal{K}_{S1}$ is less than 1%. We estimate a combined fractional uncertainty of ±0.01 in the determination of $\mathcal{K}_{S1}$ due to the precision and to uncertainties in the measurements of pressure (0.0020), temperature (0.0003), and efficiency (0.0030). We also measured $\mathcal{K}_{S2}$ for the S2 PAS mode; however, the precision for $\mathcal{K}_{S2}$ was three times larger than the precision for $\mathcal{K}_{S1}$ due to the smaller signal. We estimate that the combined fractional uncertainty for $\mathcal{K}_{S2}$ is ±0.05. After accounting for the frequency dependence of the microphone sensitivity, the measured variation in resonance width, and expected ratio of overlap integrals, both sets of $\mathcal{K}_{S1}$ and $\mathcal{K}_{S2}$ measurements
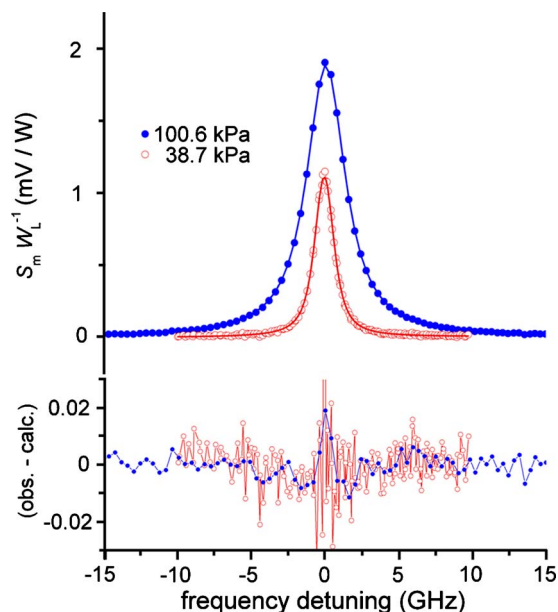
FIG. 9. (Color online) Absorption spectra of $^PP(9)$ O_2 A-band transition at two pressures probed by excitation of the S1 PAS mode. The top panel shows measurements (symbols) and respective fits (lines) of Galatry profiles, and the bottom panel gives the fit residuals. The peak signal-to-noise ratios are 486:1 and 122:1 for the high and low pressure cases, respectively.

differed by less than ±4%, which was within the combined uncertainties.

Typical measured spectra, Galatry fits to the data, and fit residuals for the $^PP(9)$ transition at $p=100.6$ and 38.7 kPa are shown in Fig. 9. The measured spectra exhibit the expected pressure-dependent width and conform well to the Galatry profile line shape. We also investigated instrumental effects on line shape by floating the Lorentzian width parameter in the fitting procedure. The fitted Lorentzian widths of the measured PA spectra were proportional to pressure and in good agreement with published values, although they were consistently smaller than the latter by 0.65%–1.4%. We observed a slow drift in the laser frequency (in the direction of the laser tuning) as the laser was step scanned over the absorption feature, which may account for the small disparity between measured and published linewidths.

Our spectrally resolved measurements illustrate that intensity-modulated PAS (IM-PAS) of isolated transitions yields the absorption line shape with minimal instrumental distortion. Schilt and Thévenaz[31] qualitatively compared IM-PAS spectra to those acquired using wavelength-modulation PAS (WM-PAS). They showed that IM-PAS reproduced qualitatively the absorption spectrum, whereas WM-PAS resembles a derivative of the spectrum. However, their IM-PAS method, which was based on current modulation of a distributed feedback diode laser, was subject to residual wavelength modulation. Measured spectra based on wavelength-modulation techniques depend on derivatives of the line shape as well as details of the laser modulation.[43,44] Unlike the present approach based on IM-PAS, these complications of WM-PAS preclude the direct measurement of intrinsic line shapes.
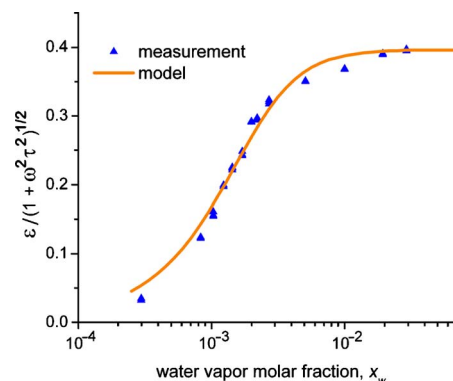

FIG. 10. (Color online) Measured and modeled PAS efficiency (S1 mode) as a function of water vapor molar fraction for $^PP(9)$ O_2 A-band transition. The solid line is a fit of Eq. (8) from which we obtained the rate constant $\kappa_{PA}/n_w=1.97\times10^{-13}$ cm^3 molecule^{-1} s^{-1}. The time constant τ_{PA} ranges from 1 ms to 6.8 μs over the experimental range of x_w. (40% RH at 20 °C corresponds to $x_w\approx0.02$.)

B. Measurements of water-mediated relaxation effects

In order to quantify variation in the PAS efficiency with water vapor concentration, we probed the peak of the O_2 A-band $^PP(9)$ transition at atmospheric pressure conditions using the S1 PAS mode. The water vapor molar fraction was varied in the range of 3×10^{-4}–3×10^{-2} (RH≈1%–90%). It was necessary to account for slight changes in the PAS resonance frequency (caused by variation in the gas composition) by measuring f_{S1} at each condition as described above. The experimental results are shown in Fig. 10 and reveal a strong dependence of PA signal strength on water vapor molar fraction. Lowering the water vapor concentration by two decades relative to the 90% relative humidity condition reduced the efficiency by more than an order of magnitude. We also measured static samples of nominally pure O_2 (at $p=110$ kPa) for which we observed weaker PA signals than in humidified air. In this case, the magnitude of the PAS response may have been influenced by residual water vapor.

The solid line in Fig. 10 gives the calculated efficiency curve obtained by least-squares fit of Eq. (8) to the experimental data. Using the values given above for the spontaneous emission coefficients, neglecting relaxation to the ground state, and assigning $\kappa_{21}=\kappa_{PA}$, we obtain $\kappa_{PA}/n_w=2.11\times10^{-13}$ cm^3 molecule^{-1} s^{-1} for the relaxation rate constant for the reaction $O_2(b\ ^1\Sigma_g^+,\ v=0)+H_2O\rightarrow O_2(a\ ^1\Delta_g,\ v=0)+H_2O(+\Delta E)$. This rate constant is approximately 30 times smaller than the literature value for κ_{ba} of 5.9×10^{-12} cm^3 molecule^{-1} s^{-1} (Ref. 42) for the reaction $O_2(b\ ^1\Sigma_g^+)+H_2O\rightarrow O_2+H_2O$. We attribute the difference to additional vibration to rotation-translation (V-RT) relaxation necessary for PA detection. The additional relaxation is required to convert the excited-state vibrational energy of the collision partner (water vapor) to heat, as depicted in Fig. 8. In the limit of high water vapor concentration, the measured efficiency reaches an asymptotic value. This measured asymptote is consistent with the O_2 energy-gap ratio $\tilde{\nu}_{ba}/\tilde{\nu}_{bX}\approx0.4$. Importantly, we note that at room temperature and typical relative humidity conditions (RH=40%), the efficiency function is within 1.2% of its asymptotic value, indicating that laboratory air is suitable as a sample gas for cali-

TABLE IV. Summary of calculated, C_c, and measured, C_m, and cell constants. The laboratory air measurements correspond to the $^P P(9)$ O_2 A-band transition.

	f_0 (Hz)	C_c (Pa cm W^{-1})	C_m (Pa cm W^{-1})	C_c/C_m
Laboratory air, S1 mode	1636.3	4569.5	4534.5	1.01 ± 0.01
Laboratory air, S2 mode	4886.6	801.9	830.6	0.97 ± 0.05
CO_2, S1 mode	1274	5894.7	5731.5	1.03 ± 0.05

brating PAS systems in terms of the O_2 A-band lines presented here.

C. Measurement validation and comparison to theoretical calculations

As a check on our system constant measurements based on the O_2 A-band spectra, we also investigated the S1 mode PAS system response by probing the $(30^0 1) \leftarrow (00^0 1)$ R16e CO_2 transition occurring at $\tilde{\nu}_0 = 6359.967$ cm^{-1} (see Ref. 45 for notation). This transition has a line intensity at 296 K equal to 1.74×10^{-23} cm molecule^{-1}.[9] The sample gas was pure CO_2, humidified with the saturator-based dilution system described above. All experimental components were the same as described above, except for the ECDL and power meter which were required for measurements in this wavelength region. These experiments indicated that the V-RT relaxation effects for the CO_2 system are efficient with relatively small amounts of added water vapor. Moreover, the asymptotic PAS conversion efficiency ε approached unity. This should be compared to the rate-limited relaxation behavior observed for the O_2 A-band spectra which gave $\varepsilon \approx 0.4$. We estimate the combined fractional uncertainty of ± 0.05 in the determination of $\mathcal{K}_{S1}$ with CO_2 due to the precision (0.01), window fouling (0.0400), efficiency (0.0030), modulation (0.0200), and to uncertainties in the measurements of pressure (0.0020) and temperature (0.0002).

Finally, we present in Table IV a summary of the calculated and measured cell constants in laboratory air (S1 and S2 modes) and in CO_2 (S1 mode). The calculated values are based on the foregoing model of the acoustic resonator, system dimensions, and fluid properties. The measured values are derived directly from the PA signal, tabulated spectroscopic parameters, and measured microphone sensitivity. The measured and modeled cell constants for the S1 mode in laboratory air differ by only 1%. For all three cases together, the measurements and calculations agree with a relative standard deviation of 0.035.

VII. CONCLUSIONS

In this paper we demonstrated that the calculated and measured cell constant of our standard PA spectrometer differ by about 1%, provided that all relevant relaxation mechanisms are properly taken into account. We note two attractive aspects of our PA cell which make it amenable to modeling. First, the system has a high degree of axial symmetry, with planar windows and no baffles, and second, the inlet and exit tubes are relatively small and located near nodal planes, thus promoting turbulent mixing of the gases and minimizing

their impact on the cell constant. These and other design simplifications make it possible to accurately calculate the cell constant from first principles. Moreover, we derived a modular solution for the PA wave functions that allows for small modifications of the microphone design to be easily taken into account. We have shown how the specific properties of the microphone (which is the most likely system component to be modified) affect the cell constant in a predictable way. The ability to accurately predict the PA cell constant (combined with an accurate calibration of the microphone sensitivity) will be useful for measuring the absorption coefficient in unknown samples. This should be true for aerosols where relaxation effects are often unimportant and where system calibrations using standard particles tend to be confounded by uncertainty in particle absorption cross section and/or number density. We have also shown that the PAS response can be conveniently calibrated in terms of the O_2 A-band spectroscopic parameters using samples of air at room temperature, pressure, and humidity conditions. We demonstrated that for PAS of the O_2 A-band, the conversion efficiency of absorbed photon energy to acoustic energy is at most 40% and strongly dependent on water vapor concentration. When calibrating in terms of A-band spectra, failure to account for this factor leads to large systematic errors in determination of the PAS system constant. We believe that the calibration technique discussed here is an attractive and convenient alternative to other approaches that may involve hazardous compounds, difficult sample preparation, difficult-to-access spectral regions, or species with uncertain absorption cross sections.

[1] A. Miklós, P. Hess, and Z. Bozoki, Rev. Sci. Instrum. **72**, 1937 (2001).
[2] W. R. Harshbarger and M. B. Robin, Acc. Chem. Res. **6**, 329 (1973).
[3] F. J. M. Harren, G. Cotti, J. Oomens, and S. Lintel Hekkert, in *Encyclopedia of Analytical Chemistry*, edited by R. A. Meyers (Wiley, Chichester, 2000), pp. 2203–2226.
[4] K. M. Adams, Appl. Opt. **27**, 4052 (1988); K. M. Adams, L. I. Davis, S. M. Japar, and W. R. Pierson, Atmos. Environ. **23**, 693 (1989).
[5] W. P. Arnott, H. Moosmüller, and J. W. Walker, Rev. Sci. Instrum. **71**, 4545 (2000).
[6] A. A. Kosterev, T. S. Mosely, and F. K. Tittel, Appl. Phys. B: Lasers Opt. **85**, 295 (2006).
[7] S. Schilt, J.-P. Besson, and L. Thévenaz, Appl. Phys. B: Lasers Opt. **82**, 319 (2006).
[8] J.-P. Besson, S. Schilt, and L. Thévenaz, Appl. Phys. B: Lasers Opt. **90**, 191 (2008).
[9] L. S. Rothman, I. E. Gordon, A. Barbe, D. C. Benner, P. E. Bernath, M. Birk, V. Boudon, L. R. Brown, A. Camparque, J. P. Champion, K. Chance, L. H. Coudert, V. Dana, V. M. Devi, S. Fally, J. M. Flaud, R. R. Gamache, A. Goldman, D. Jacquemart, I. Kleiner, N. Lacome, W. J. Lafferty, J. Y. Mandin, S. T. Massie, S. N. Mikhailenko, C. E. Miller, N. Moazzen-Ahmadi, O. V. Naumenko, A. V. Nikitin, J. Orphal, V. I. Perevalov, A. Perrin, A. Predoi-Cross, C. P. Rinsland, M. Rotger, M. Simeckova, M. A. H. Smith, K. Sung, S. A. Tashkun, J. Tennyson, R. A. Toth, A. C. Vandaele, and J. Vander Auwera, J. Quant. Spectrosc. Radiat. Transf. **110**, 533 (2009).

[10] D. K. Havey, D. A. Long, M. Okumura, C. E. Miller, and J. T. Hodges, Chem. Phys. Lett. **483**, 49 (2009).

[11] D. J. Robichaud, J. T. Hodges, L. R. Brown, D. Lisak, M. Okumura, and C. E. Miller, J. Mol. Spectrosc. **248**, 1 (2008).

[12] G. Tian, H. Moosmüller, and W. P. Arnott, Aerosp. Sci. Technol. **43**, 1084 (2009).

[13] Under review by NIST patent advisors.

[14] A. Rosencwaig, *Photoacoustics and Photoacoustic Spectroscopy* (Wiley, New York, 1980).

[15] P. Hess, *Photoacoustic, Photothermal, and Photochemical Processes in Gases* (Springer-Verlag, Berlin, 1989).

[16] P. M. Morse and K. U. Ingard, *Theoretical Acoustics* (McGraw-Hill, New York, 1968).

[17] J. P. M. Trusler, *Physical Acoustics and Metrology of Fluids* (Adam-Hilger, Bristol, 1991).

[18] ISO 9613-1:1993, International Organization for Standardization, 1993.

[19] M. R. Moldover, J. B. Mehl, and M. Greenspan, J. Acoust. Soc. Am. **79**, 253 (1986).

[20] F. G. C. Bijnen, J. Reuss, and F. J. M. Harren, Rev. Sci. Instrum. **67**, 2914 (1996).

[21] In order to describe materials and experimental procedures adequately, it is occasionally necessary to identify commercial products by the manufacturer's name or label. In no instance does such identification imply endorsement by the National Institute of Standards and Technology, nor does it imply that the particular product or equipment is necessarily the best available for the purpose.

[22] M. R. Moldover, J. P. M. Trusler, T. J. Edwards, J. B. Mehl, and R. S. Davis, J. Res. Natl. Bur. Stand. **93**, 85 (1988).

[23] E. W. Lemmon, M. O. McLinden, and M. L. Huber, *NIST Standard Reference Data Base 23: Reference Fluid Thermodynamic and Transport Properties, Version 8.0* (National Institute for Standards and Technology, Standard Reference Data Program, Gaithersburg, MD, 2002).

[24] I. B. Crandall, *Theory of Vibrating Systems and Sound* (Van Nostrand, New York, 1927), pp. 229–241.

[25] K. A. Gillis, J. B. Mehl, and M. R. Moldover, J. Acoust. Soc. Am. **114**, 166 (2003).

[26] F. B. Daniels, J. Acoust. Soc. Am. **19**, 569 (1947).

[27] J. B. Mehl, J. Acoust. Soc. Am. **106**, 73 (1999).

[28] B. van Diedenhoven, O. P. Hasekamp, and I. Aben, Atmos. Chem. Phys. **5**, 2109 (2005).

[29] K. Chance, J. Quant. Spectrosc. Radiat. Transf. **58**, 375 (1997).

[30] C. R. Nowlan, C. T. McElroy, and J. R. Drummond, J. Quant. Spectrosc. Radiat. Transf. **108**, 371 (2007).

[31] S. Schilt and L. Thévenaz, Infrared Phys. Technol. **48**, 154 (2006).

[32] D. W. Allan, Proc. IEEE **54**, 221 (1966).

[33] L. Galatry, Phys. Rev. **122**, 1218 (1961).

[34] P. L. Varghese and R. K. Hanson, Appl. Opt. **23**, 2376 (1984).

[35] B. F. Minaev and V. A. Minaeva, Phys. Chem. Chem. Phys. **3**, 720 (2001).

[36] K. J. Ritter and T. D. Wilkerson, J. Mol. Spectrosc. **121**, 1 (1987).

[37] N. P. Vagin, A. A. Ionin, I. V. Kochetov, A. P. Napartovich, Y. P. Podmar'kov, M. P. Frolov, and N. N. Yuryshev, Quantum Electron. **35**, 378 (2005).

[38] H. C. Miller, J. E. McCord, J. Choy, and G. D. Hager, J. Quant. Spectrosc. Radiat. Transf. **69**, 305 (2001).

[39] C. Schweitzer and R. Schmidt, Chem. Rev. (Washington, D.C.) **103**, 1685 (2003).

[40] J. P. Singh, J. Bachar, D. W. Setser, and S. Rosenwaks, J. Phys. Chem. **89**, 5347 (1985).

[41] J. P. Singh and D. W. Setser, J. Phys. Chem. **89**, 5353 (1985).

[42] S. P. Sander, B. J. Finlayson-Pitts, R. R. Friedl, D. M. Golden, R. E. Huie, H. Keller-Rudek, C. E. Kolb, M. J. Kurylo, M. J. Molina, G. K. Moortgat, V. L. Orkin, A. R. Ravishankara, and P. H. Wine, *Chemical Kinetics and Photochemical Data for Use in Atmospheric Studies* (Jet Propulsion Laboratory, Pasadena, 2006), Evaluation No. 15, JPL Publication No. 06-2.

[43] R. Arndt, J. Appl. Phys. **36**, 2522 (1965).

[44] S. Schilt, L. Thévenaz, and P. Robert, Appl. Opt. **42**, 6728 (2003).

[45] R. A. Toth, L. R. Brown, C. E. Miller, V. Malathy Devi, and D. C. Benner, J. Quant. Spectrosc. Radiat. Transf. **109**, 906 (2008).